PASJ: Publ. Astron. Soc. Japan , 1–??,

X-Ray Imaging Spectrometers(XIS) on Board Suzaku

Katsuji KOYAMA[1], Hiroshi TSUNEMI[2], Tadayasu DOTANI[3], Mark W. BAUTZ[4]
Kiyoshi HAYASHIDA[2], Takeshi TSURU[1], Hironori MATSUMOTO[1], Yoshiaki OGAWARA[3],
George R. RICKER[4], John DOTY[12], Steven E. KISSEL[4], Rick FOSTER[4] , Hiroshi NAKAJIMA[1],
Hiroya YAMAGUCHI[1], Hideyuki MORI[1], Masaaki SAKANO[1], Kenji HAMAGUCHI[1], Mamiko NISHIUCHI[1],
Emi MIYATA[2], Ken′ichi TORII[2], Masaaki NAMIKI[2], Satoru KATSUDA[2],
Daisuke MATSUURA[2], Tomofumi, MIYAUCHI[2], Naohisa ANABUKI[2], Noriaki TAWA[2],
Masanobu OZAKI[3], Hiroshi MURAKAMI[3], Yoshitomo MAEDA[3],
Yoshinori ICHIKAWA[3], Gregory Y. PRIGOZHIN[4], Edward A. BOUGHAN[4], Beverly LAMARR[4], Eric D. MILLER[4]
Barry E. BURKE[5], James A. GREGORY[5], Allen PILLSBURY[5], Aya BAMBA[6], Junko S. HIRAGA[6],
Atsushi SENDA[6], Haruyoshi KATAYAMA[7], Shunji KITAMOTO[8], Masahiro TSUJIMOTO[8], Takayoshi KOHMURA[9],
Yohko TSUBOI[10] & Hisamitsu AWAKI[11]

[1]*Department of Physics, Graduate School of Science, Kyoto University, Kita-Shirakawa, Sakyo-ku, Kyoto 606-8502*
koyama@cr.scphys.kyoto-u.ac.jp
[2]*Department of Earth and Space Science, Graduate School of Science , Osaka University, 1-1 Machikane-yama, Toyonaka, Osaka 560-0043*
[3]*Institute of Space and Astronautical Science, Japan Aerospace Exploration Agency, 3-1-1 Yoshino-dai, Sagamihara, Kanagawa 229-8510*
[4]*Kavli Institute for Astrophysics and Space Research, Massachusetts Institute of Technology, Cambridge, MA 02139, USA*
[5]*Massachusetts Institute of Technology, Lincoln Laboratory, Lexington, MA, USA*
[6]*The Institute of Physical and Chemical Research (RIKEN), 2-1 Hirosawa, Wako, Saitama 351-0198*
[7]*Japan Aerospace Exploration Agency (JAXA), 2-1-1 Sengen, Tsukuba, Ibaraki 305-8505*
[8]*Department of Physics, Faculty of Science, Rikkyo University, 3-34-1 Nishi-Ikebukuro, Toshima-ku, Tokyo 171-8501*
[9]*Physics Department, Kogakuin University, 2665-1 Nakano-cho, Hachioji, Tokyo 192-0015*
[10]*Department of Physics, Faculty of Science and Engineering, Chuo University, 1-13-27 Kasuga, Bunkyo-ku, Tokyo 112-8551*
[11]*Department of Physics, Faculty of Science, Ehime University, Bunkyo-cho, Matsuyama, Ehime 790-8577*
[12]*Noqsi Aerospace Ltd, 2822 South Nova Road, Pine, Colorado 80470, USA*

(Received 2006 July 5; accepted 2006 August 14)

Abstract

The XIS is an X-ray Imaging Spectrometer system, consisting of state-of-the-art charge-coupled devices (CCD) optimized for X-ray detection, camera bodies and control electronics. Four sets of XIS sensors are placed at the focal planes of the grazing-incidence, nested thin-foil mirrors (XRT: X-Ray Telescope) onboard the Suzaku satellite. Three of the XIS sensors have front-illuminated (FI) CCDs, while the other has a back-illuminated (BI) CCD. Coupled with the XRT, the energy range of 0.2–12 keV with energy resolution of 130 eV at 5.9 keV, and a field of view of $18' \times 18'$ are realized. Since the Suzaku launch on 10 July 2005, the XIS has been functioning well.

Key words: instrumentation: detectors—methods: data analysis—space vehicles—X-ray CCDs

1. Introduction

Astro-E was launched on 10 February 2000 with the M-V rocket from Kagoshima Space Center, but was lost due to the failure of the first stage motor. After 5 years, the re-flight mission, Astro-EII, was successfully put into a near-Earth orbit on 10 July 2005, and named Suzaku (Mitsuda et al. 2006). One of the main instruments on Suzaku is the X-ray Imaging Spectrometer (XIS), comprised of four X-ray charge-coupled devices (CCD) each placed at the focus of a dedicated X-Ray Telescope (XRT) (Serlemitsos et al. 2006).

The first successful space flight use of X-ray CCDs as photon counting and spectroscopic imagers was with the SIS units (Burke et al. 1991) on ASCA. Since then, X-ray CCDs have become standard focal plane detectors for X-ray telescopes, and have been adopted as the principal detector of recent X-ray observatories, such as Chandra (Weisskopf et al. 2002), and XMM (Lumb et al. 2000). Based on the ASCA and Astro-E experiences, the XIS has been re-designed for better performance. Major improvements from the ASCA SIS are: (1) thicker depletion layer ($\sim 65\mu$m), (2) lower operating temperature (-90°C) to reduce the effects of radiation damage, (3) pixel-level determination of dark-level, (4) greater flexibility in the CCD clocking scheme, and (5) larger area (5×5 pixel) for X-ray event extraction. Advantages compared with the Chandra ACIS, and the XMM-Newton EPIC are: (1)

a precision charge injection (CI) capability to mitigate effects of radiation damage, and (2) a chemisorption surface treatment (Lesser and Lyer 1998) on the back-illuminated (BI) CCD for improved charge collection and spectral resolution.

This paper describes the basic design, fabrication, control and data processing system, on ground calibration and on-orbit performance of the XIS. Early reports on the XIS system and on-ground calibration are found in Dotani et al. (2003), Matsumoto et al. (2005), and references therein.

2. Mechanical and Thermal Structure of the XIS

A photograph of the XIS sensor (CCD+camera body) is shown in figure 1, while the cross section is shown in figure 2. The XIS camera body consists of (from top to bottom in figure 2) a hood, bonnet and base. The hood has five baffles to block stray light. The bonnet includes a vacuum valve, an optical blocking filter (OBF), calibration sources (^{55}Fe), a pressure sensor, a paraffin actuator and a door. The base contains an X-ray CCD mounted on an alumina (Al_2O_3) substrate and is attached to a heat sink assembly made of copper (Cu). A Peltier cooler incorporated in the heat sink can cool the detector to its on-orbit operating temperature of -90°C. Over the frame-store region of the CCD, an aluminum (Al) shield with a gold (Au)-plated nickel (Ni) surface treatment is placed to block X-ray irradiation. The surfaces of the substrate, the heat sink assembly and the shield are also plated with Au. The bonnet and the hood are made of Al with black surface finish. The inside of the base is Ni-plated, except for the feed-through plate which is Au electro-plated. The XIS sensor is covered by multi-layer insulators to reduce heat-flow from the satellite body.

The XIS sensor has an electric valve, mainly used to evacuate the base during ground testing before launch. The body is kept at vacuum during launch to protect the fragile OBF from acoustic vibration. A pressure sensor is installed in the body to monitor the internal pressure. The valve was opened immediately after the launch to evacuate the body to sufficiently high vacuum and to allow cooling the CCD detectors. Then the valve was closed again to prevent possible contamination on the CCD from the thruster fuel during the perigee-up operation. The non-X-ray background (NXBG) data and calibration data from the door-attached sources were accumulated in the door-closed configuration for 18 days. The door was then opened by the paraffin actuator.

2.1. *Calibration Source*

Each XIS sensor has three ^{55}Fe calibration sources. One is attached to the door, and illuminates the whole imaging area (IA: see section 2.3). This calibration source was used on the ground and for initial on-orbit calibration before the door was opened. For normal observation, after the door is open, this calibration source is out of the field of view of the CCD. The other two calibration sources are

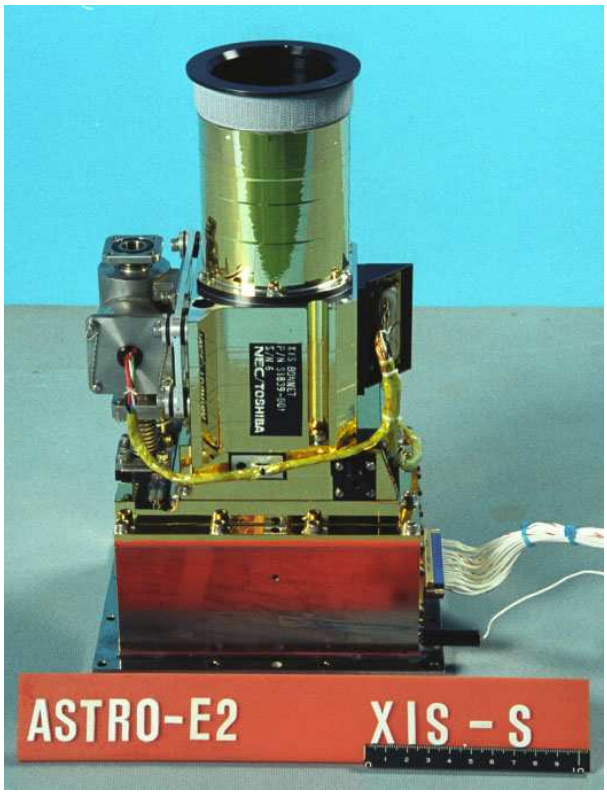

Fig. 1. A picture of the XIS sensor.

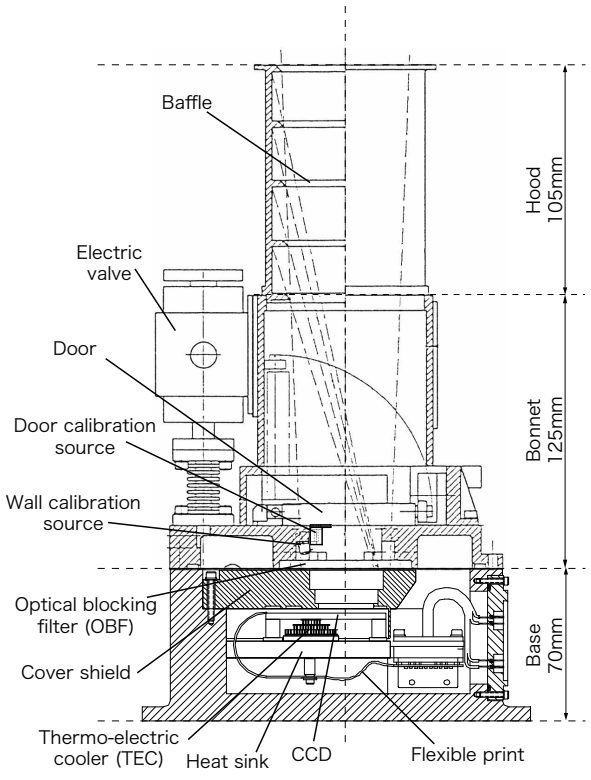

Fig. 2. Cross section of the XIS sensor.

located on a side wall of the bonnet and illuminate the two far-end corners (from the read-out node) of the IA. The fluxes of the calibration sources were selected so that the gain can be determined at 5.9 keV with a statistical error of 0.1% within a single orbit early in the mission.

2.2. Optical Blocking Filter

The XIS CCDs are sensitive to optical and UV light, and hence have optical blocking filters (OBF) 20mm above the IA. The OBF is made of a polyimide ($C_{22}H_{10}N_2O_4$) film with vapor-deposited Al on both sides, in order to avoid light leakage from pinholes. The thicknesses of the Al on the two sides of the filter are different from each other. This reduces the light transmission by the interference effect (Born and Wolf 1999). The thicknesses of the polyimide film and the Al layers are ∼1400Å and ∼800Å + 400Å respectively. The OBF has a low transmission coefficient for optical light ($\leq 5 \times 10^{-5}$), but is transparent to X-rays ($\geq$ 80 % above 0.7 keV). The measured transmissions for optical light and soft X-rays are reported in Kitamoto et al. (2003).

2.3. X-Ray CCDs

The XIS has four sensors (XIS0 through XIS3), and each sensor has one CCD chip, which is a MOS-type three-phase CCD operated in the frame transfer mode. A schematic view of the CCD can be seen in figure 3. The CCD consists of four segments (A, B, C and D), each with a dedicated read-out node. Three sensors (XIS0, 2 and 3) contain front-illuminated (FI) CCDs and the other (XIS1) has a back-illuminated (BI) CCD. Since the front side of the CCD has a gate structure made of thin Si and SiO_2 layers, the FI CCD is less sensitive than the BI CCD to soft X-rays. A simplified model of the dead layers in the FI devices, in which the gate structure is approximated as a stack of nearly uniform slabs, has been fit to the ground calibration data. Then the dead layer thicknesses of $\sim 0.28\mu$m (Si) and $\sim 0.44\mu$m (SiO_2) are inferred. The surface dead layers of the BI CCD is very thin, consisting of 5nm HfO_2, 1nm Ag, and 3nm SiO_2. However, the quantum efficiency (QE) of the BI CCD is also affected by imperfect charge collection efficiency near the back surface of the silicon, which has not been fully characterized as of this writing. The BI CCD has a thinner depletion layer ($\sim 42\mu$m) than the FI CCDs ($\sim 65\mu$m). Therefore the QE of the BI CCD at high energy is lower than the FI CCDs. The QEs for the FI and BI CCDs, are shown as a function of energy in figure 4.

A chemisorption charging process developed at the University of Arizona is applied to the BI CCD. This process improves the charge collection efficiency near the back (X-ray illuminated) surface, and hence provides the nearly the same energy resolution of the FI CCDs even in soft X-rays. Details on the application of the chemisorption charging process are found in Lesser and Lyer (1998).

The imaging area (IA) of the CCD has 1024×1024 pixels. The pixel size is 24 μm × 24 μm, giving a size of 25 mm × 25 mm for the IA. The IA, combined with the XRT, covers an $18' \times 18'$ region on the sky. The

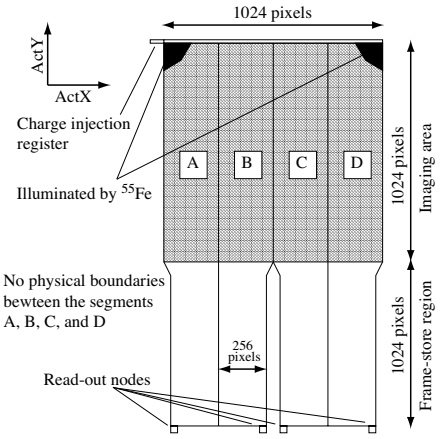

Fig. 3. Schematic view of the XIS CCD (top view). The CCD consists of four segments (A, B, C and D), each with a dedicated read-out node.

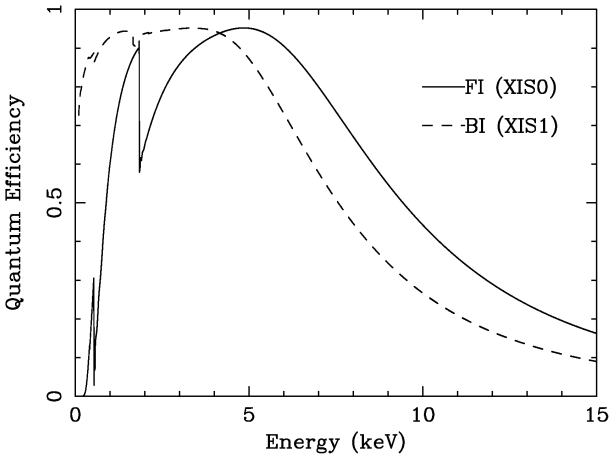

Fig. 4. The QE as a function of incident energy, calculated using best estimate values of the thickness of dead layers and depletion layer. The solid line represents the FI CCD (XIS0) and the broken line is for the BI CCD (XIS1).

specification of the XIS CCD combined with the OBF and XRT is summarized in Table 1. Position in the IA is defined by the detector-fixed coordinates (ActX, ActY), where the origin (0, 0) is taken to be the first pixel read-out of segment A in normal clocking mode (clocking modes are defined below in section 3.2). The positive directions are shown by arrows in figure 3. In the IA, ActX runs from 0 to 1023 (from segment A to D), while ActY runs from 0 to 1023 (from the read-out node to the charge injection register). The four XIS sensors are placed on the focal planes of the four X-ray telescopes (XRT), in different orientations with respect to the satellite coordinate system; the ActX axes of XIS0 and 3 are anti-parallel to the satellite X-axis, while those of XIS1 and 2 are anti-parallel and parallel to the satellite Y-axis, respectively.

Table 1. Specifications/Characteristics of the XIS CCD combined with the OBF and XRT.

Field of View	$18' \times 18'$
Energy Range	0.2–12 keV
Format	1024× 1024 pixels
Pixel Size	24 μm × 24 μm
Energy Resolution	∼ 130 eV (FWHM) at 5.9 keV
Effective Area[a]	
(1.5 keV)	330 cm^2 (FI[b]), 370 cm^2 (BI[c])
(8 keV)	160 cm^2 (FI[b]), 110 cm^2 (BI[c])
Readout Noise	∼2.5 electrons (RMS)
Time Resolution	8 s (normal), 7.8ms (P-sum)

a: On-axis effective area for one sensor including the OBF transmission, the CCD quantum efficiency, and the XRT effective area. The calculations are for a point source integrated over a circular region with a 6 mm (4.34 arc min) radius.
b: Front-illuminated CCD.
c: Back-illuminated CCD.

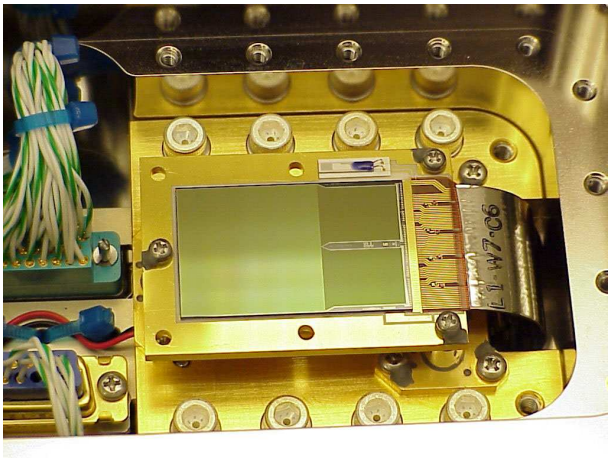

Fig. 5. The CCD and heat sink assembly installed in the base. The cover shield is removed in this picture.

2.4. Heat Sink and Thermo-Electric Cooler (TEC)

A three-stage thermo-electric cooler (TEC) is used to cool the CCD to the nominal operating temperature of −90°C. The cold-end of the TEC is directly connected to the substrate of the CCD, which is mechanically supported by 3 Torlon (polyamide-imide plastic) posts attached to the heat sink. The heat is transferred through a heat pipe to a radiator panel on the satellite surface, and is radiated away to space. The radiator and the heat pipe are designed to cool the base below −40°C under the nominal TEC operating conditions. Figure 5 is a photograph of the inside of base with the frame-store cover shield removed. Since the TEC is placed under the CCD, and the heat pipe is running under the base plate, these are not seen in figure 5.

2.5. Radiation Shield

The performance of any CCD gradually degrades due to radiation damage in orbit. For satellites in low-Earth orbit like Suzaku, most of the damage is due to large fluxes of charged particles in the South Atlantic Anomaly (SAA). The radiation damage increases the dark current, and the charge transfer inefficiency (CTI). The XIS sensor body provides radiation shielding around the CCD. We found from the ASCA SIS experiment that radiation shielding of > 10 g cm^{-2} equivalent Al thickness is required. The proton flux density at 2 MeV on the CCD chip through 10 g cm^{-2} of shielding is estimated to be $\sim 2 \times 10^3$ protons cm^{-2} MeV^{-1} day^{-1} in the Suzaku orbit (same as the ASCA orbit) at solar minimum.

3. On-board Data Processing

3.1. XIS electronics

The XIS control and processing electronics consist of AE/TCE (analog electronics/TEC control electronics) and DE (digital electronics). The DE is further divided into PPU (pixel processing unit) and MPU (main processing unit). Two sets of AE/TCE are installed in each of two boxes, respectively, called AE/TCE01 and AE/TCE23. Similarly, 4 PPU are housed in pairs, and are designated PPU01 and PPU23, respectively. AE/TCE01 and PPU01 jointly take care of XIS0 and XIS1, while AE/TCE23 and PPU23 are for XIS2 and XIS3. One unit of MPU is connected to all the AE/TCEs and PPUs

The AE/TCE provides the CCD clock signals, controls the CCD temperature, and processes the video signals from the CCD to create the digital data. The clock signals are generated in the AE with a step of 1/48 pixel cycle (∼ 0.5 μs) according a micro-code program, which is uploaded from the ground. The pixel rate is fixed at 24.4 μs pixel^{-1}. Therefore one line, consisting of 4 under-clocked pixels, 256 active pixels, and 16 over-clocked pixels, is read out in about 6.7 ms. The CCD output is sampled with 16-bit precision, but only 12 bits are sent to the PPU. The 12 bits are selected to cover the full energy scale of ≃15 keV in the normal setting of the gain. The full energy scale of ≃60 keV can also be selected in the low gain mode.

The AE/TCE controls the TEC (thermo-electric cooler) to generate a temperature difference of ∼ 50°C relative to the base, while keeping the CCD chip at −90°C. The AE/TCE can also supply reverse current to the TEC, to warm up the CCD chip in orbit. The CCD temperature may be raised a few tens of °C above that of the base. In practice, the requirement to avoid excessive mechanical stresses due to differential thermal expansion of the copper heat sink relative to the alumina CCD substrate imposes an upper limit on CCD temperature in this mode. For example, with the heat sink at a typical operating temperature of −35°C, we have adopted a maximum allowable CCD temperature of about +15°C. The CCD temperature upper limit is higher at higher heat sink temperatures.

The PPU extracts a charge pattern characteristic of X-

rays, called an event, after applying various corrections to the digital data supplied by the AE/TCE. Extracted event data are sent to the MPU. Details of the event extraction process are described in section 3.3. The PPU first stores the data from its AE/TCE in a memory called the pixel RAM. In this process, copied and dummy pixels [1] are inserted in order to avoid a gap in the event data at segment boundaries, to ensure proper event extraction at segment boundaries and to enable identical processing of all segments of the data. The raw data from AE/TCE may include a pulse height (PH) offset from the true zero level due to dark current, small light leakage through the OBF, and/or an electric offset. Since the offsets depend on the CCD position and time, offset corrections are also position and time dependent. To reduce the computing power and time required for such corrections, the offsets are divided into two parts, dark-level and light-leak. The dark-level is the average output from a pixel with no irradiation of X-rays or charged particles. The dark-level is determined for individual pixels, and is up-dated by command only after each SAA passage in the normal clocking mode. On the other hand, the dark-level is continuously up-dated in the parallel-sum clocking mode (P-sum, hereafter). For the dark-level calculation, the PPU identifies pixels whose PH exceeds a pre-defined threshold, and registers them as hot pixels. Hot pixels are excluded from the subsequent event extraction process.

The light-leak is defined in a block region of 64×64[2] pixels and is up-dated frame by frame to compensate rapid (but nearly uniform in position) changes of the PH offset. No light-leak is defined in the P-sum mode because it is effectively included in the dark-level (see section 3.2).

The MPU works as a command-decoder, PPU and AE/TCE controller and a telemetry generator. The MPU collects the event data or diagnostic data from the PPU and the housekeeping data from the AE/TCE, compiles them in telemetry format and sends them to the satellite data processor (DP).

3.2. The clocking modes

A proper XIS clocking scheme is required for the observation of each X-ray source. The clocks are generated by the sequencer in the AE according to the micro-code. Although the sequencer is very flexible, a limited number of clocking modes are used in practice to simplify the subsequent signal processing. The basic clocking modes are normal and P-sum mode. The former can produce a two-dimensional CCD image, while the latter compresses the image into one-dimension. Two options, called burst and window options, are available in normal mode.

The normal mode with no option reads all the pixels in the CCD every 8 sec. Hence, the normal mode produces 1024×1024-pixel data. This mode is most frequently used for X-ray observations. The burst option selects the exposure time arbitrarily (in 1/32 sec steps) within the readout interval of 8 sec and provides a full-sized image. This option introduces an artificial dead time; if the exposure is t s, a dead time of $(8 - t)$ sec is introduced every 8 sec. This option is used for observations of bright, especially extended sources to avoid photon pile-up. The window option reads only a selected part of the CCD IA, called a window. The window has the full width of the CCD X-direction (ActX), but its Y-direction (ActY) size is limited to 256, 128, or 64 rows. The window can be located arbitrarily along ActY (see figure 3). Depending on the window size, the exposure time becomes 2 sec, 1 sec, or 0.5 sec. This option is used for bright point sources. The window and the burst options can be applied simultaneously. This is especially useful for very bright sources to avoid photon pile-up.

The P-sum mode sums multiple rows (64, 128, or 256 rows) of data at the bottom of the imaging region. The 1-dimensional data are then transferred through the frame-store region to the read-out nodes. Because the 1024 rows of data are read in 8 sec, time resolution in the P-sum mode is 7.8125 ms. Subsequent data processing is done for each row of data independently. Because of the short exposure and the 1-dimensional nature of the data, P-sum mode suffers very little photon pile-up.

3.3. The editing modes

Four editing modes (5×5, 3×3, and 2×2 and timing mode) are used for X-ray observations. Three (5×5, 3×3, and 2×2) are used in combination with the normal clocking mode, while the other (timing mode) is used in the P-sum mode. The 5×5, 3×3, and 2×2 modes are designed to allow different combinations of the amount of PH information and data volume. The 5×5 mode requires the largest telemetry capacity, while 2×2 requires the least.

When an X-ray photon is absorbed in the depletion layer, it produces a charge cloud much smaller than the pixel size of the CCD ($24 \times 24 \mu$m). Thus the charge does not occupy more than 2×2 pixels. In contrast, a charged particle excites free electrons along its track, producing a larger charge cloud. Utilizing this difference, most of the charged particle events are removed. The PPU extracts events from the pixel data after applying the dark-level and light-leak corrections. An event is recognized when a pixel has a PH between the lower and upper event thresholds (a valid PH) and the PH is a local maximum among adjacent 3×3 pixels (the event center). The algorithm to search for events is common for 5×5, 3×3, and 2×2 modes. The local PH data from the neighborhood of the event center pixel are formatted according to the editing mode and are sent to the telemetry data stream.

[1] The data of each CCD segment are transferred through independent lines from the AE/TCE to the PPU, and are processed in parallel by the same processing scheme in the PPU. For a proper event extraction at the segment boundary, the data in the two columns of the adjacent CCD segment must be used. Therefore hard-wired logic is installed to "copy" the two column data in the adjacent CCD segments to the proper locations in the PPU pixel RAM. These are called as "copied pixels". In the case of outer boundaries of segments A and D, such "copied pixels" can not be prepared. Instead, two columns of zero data are prepared in the PPU pixel RAM. These are called "dummy pixels" in the PPU pixel RAM.

[2] The size was changed to 256×114 pixels after January 20, 2006

In the 5×5 mode, all the PHs of the 25 (5×5) pixels around the event center pixel are sent to the telemetry, along with each of their X, Y-coordinates of the event. The 3×3 mode sends the PHs of the 9 (3×3) pixels used for the event search together with the X, Y-coordinates. It also sends summary information on the surrounding 16 pixels: 1-bit (PH larger than a threshold or not) for each pixel and the total PH of the pixels below the threshold. The 2×2 mode extracts 4 (2×2) pixels from the 3×3 region, including the event center, the 2nd highest pixel in the cross centered at the event center, and the 3rd (or 4th) highest pixel in the cross. X, Y-coordinates, locations of the 2×2 pixels relative to the event center, and summary information of the surrounding pixels are also sent to the telemetry. The summary information includes 1-bit (PH larger than a threshold or not) for each of the 8-attached pixels, but not the total PH.

The timing mode can only be used in combination with the P-sum clocking mode. The P-sum/timing mode produces only one-dimensional data, hence the event is defined in 1×3 pixels; an event is searched for in each row independently and is recognized when a pixel has a valid PH and the PH is a local maximum within 1×3 pixels. Total PH, position, and the grade of the event are sent to the telemetry. Four grades are defined in the timing mode, i.e. single, leading/trailing split, and others, depending on the charge split pattern. Total PH is calculated by summing up at most 3 pixels according to the grade.

The 5×5 and 3×3 modes send enough PH information for on-ground corrections of charge trailing (see section 5.1) and zero level. However, the others (2×2, and timing modes) send limited PH information, hence such corrections cannot be applied.

4. Pre-Flight Calibration and Experiment

The CCD chip level calibration was done using various fluorescent X-ray sources at 16 energies in the spectral range between 0.28 keV to 11.0 keV. The photon flux produced by these sources was in turn determined using CCD reference detectors that were absolutely calibrated by means of synchrotron radiation at the PTB beam line at the BESSY electron storage ring. Details of the reference detector calibration are provided in Bautz et al. (2000), and details of the chip-level calibration are summarized in LaMarr et al. (2004). Further pre-flight calibrations of the integrated XIS sensors were made in the low energy band (0.2–2.2 keV, Hayashida et al. 2004) and in the high energy band (1.5–12.5 keV, Nakajima et al. 2005), separately.

For the soft energy calibration, a grating spectrometer was used, which covers the 0.2–2.2 keV energy band continuously. Details of the spectrometer system are described in Hashimotodani et al. (1998). In the high energy range, fluorescent X-rays from six materials (Al, Cl, Ti, Fe, Zn, and Se), and the radio isotope (^{55}Fe) were used. The line energies are 1.487, 2.622, 4.509, 6.400, 8.631, 11.208, 5.895 keV (Kα lines), and 1.557, 2.816, 4.932, 7.058, 9.572, 12.496, 6.490 keV (Kβ lines) (Hamaguchi et al. 2000).

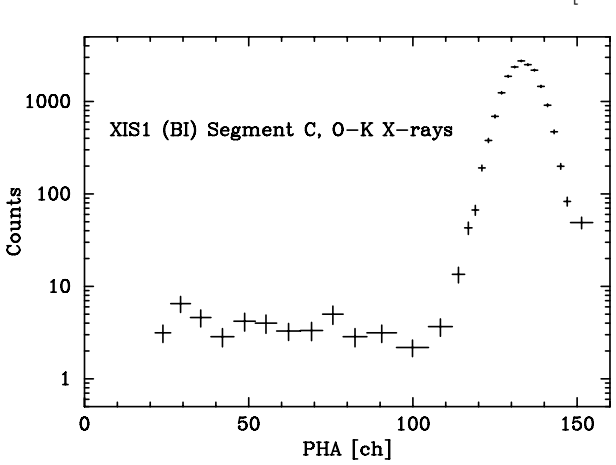

Fig. 6. Pulse height distribution of the BI (XIS1 Segment C) for the oxygen Kα line.

All the calibration data are processed using standard methods for dark-level and light-leak subtraction, and for X-ray event extraction using the ASCA grades of 0, 2, 3, 4, and 6. The split threshold is optimized to a fixed value for the FI-CCD. For the BI-CCD, the split threshold depends on the X-ray energy (Yamaguchi et al. 2005). This variable split threshold optimizes the energy resolution and quantum efficiency in the full energy range of the BI.

4.1. Pulse Height Distribution Function

Figure 6 demonstrates the excellent performance of the BI CCD at the oxygen Kα energy (0.525 keV). The energy resolution is $\sim$50 eV (FWHM) with no large low energy tail. This value is comparable to that of the FI CCD of $\sim$40 eV (FWHM). The spectral shape is similar to that of the FI CCD in the entire energy band.

In detail, the spectral shape is not a simple Gaussian but is more complicated as is shown in figure 7 for the case of ^{55}Fe (5.895 keV and 6.490 keV). The spectrum has a main peak as well as many other structures as is shown schematically in figure 8. These include the (1) main peak, (2) sub peak, (3) triangle component, (4) silicon escape peak, (5) silicon fluorescent peak and (6) constant components. In the energy range below the Si K-edge (1.839 keV), components (4) and (5) are absent. Also the triangle component does not appear in the BI CCD. The physical interpretations of these components are discussed in Matsumoto et al. (2006). The intensity ratios among the components depend on the X-ray energy, the gate structure, the depth of the depletion layer and other operating conditions. We have made an empirical model to include all these effects.

4.2. Energy Scale Linearity

We define the gain to be the ratio of the incident X-ray energy to the PH channel at the center of the main peak. For the gain calculation, we fit the PH distributions around the main peak with a two-Gaussian (main peak +

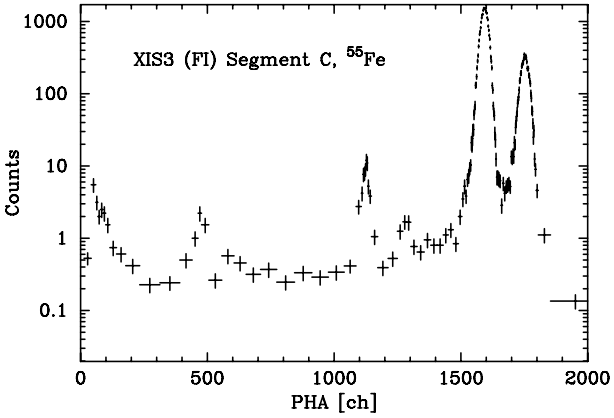

Fig. 7. Pulse height distribution of the FI (XIS3 Segment C) for the Mn Kα and Kβ lines.

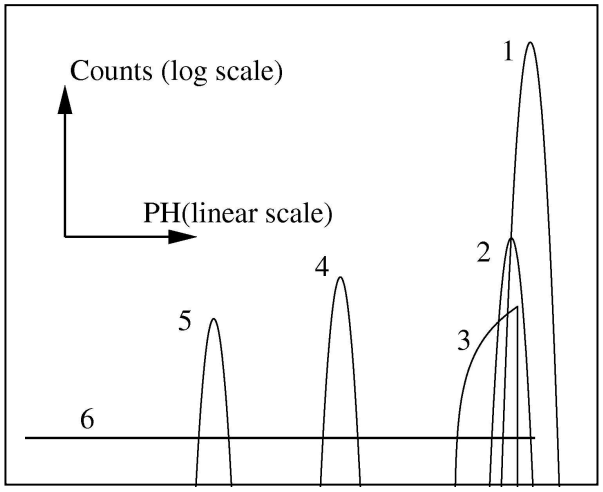

Fig. 8. Schematic picture of the response function. It consists of (1) main peak, (2) sub peak, (3) triangle component, (4) silicon escape peak, (5) silicon fluorescent peak and (6) constant tail component.

sub peak) model. The relation between the X-ray energy and the PH of the main peak is plotted in figure 9. We fit a linear function to the data and found an apparent deviation at the Si-K edge (1.839 keV). We therefore applied two different linear functions below and above 1.839 keV, respectively. The best fit results are given by the solid line in figure 9. The energy deviation of the data from the best-fit model is less than ∼0.5% in the full energy range for all the sensors and segments.

4.3. Energy Resolution

The energy resolution is defined as the full width at half maximum (FWHM) of the Gaussian function of the main peak. Figure 10 shows the energy resolution as a function of incident X-ray energy. The energy resolution of an X-ray CCD is expressed as;

$$\Delta E(eV) = W \times \sqrt{8\ln 2} \times \sqrt{N^2 + \frac{EF}{W} + AE^2}, \qquad (1)$$

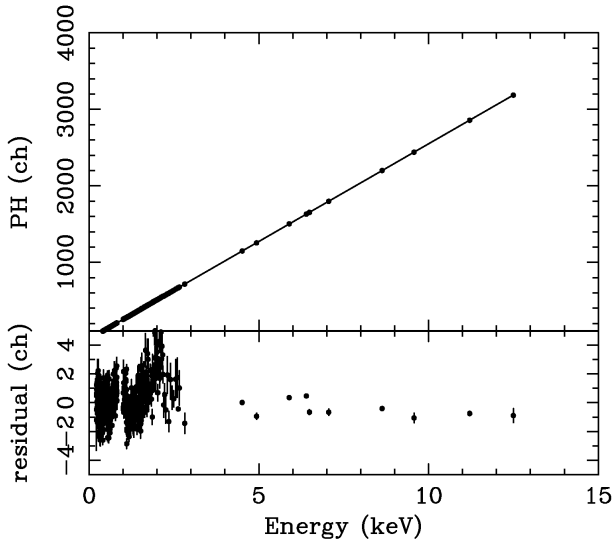

Fig. 9. The energy-PH relation for the BI (XIS1 Segment C).

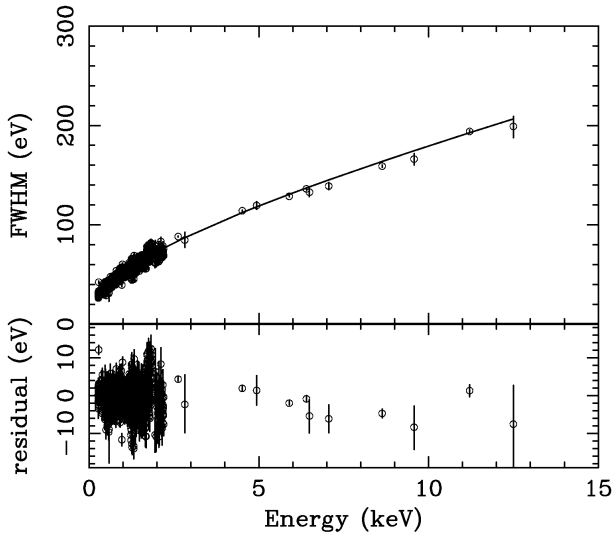

Fig. 10. The energy resolution as a function of energy for the FI (XIS2 Segment C).

where E, F, W, N and A are the X-ray energy in eV, the Fano factor, the mean energy for electron-hole pair creation in Si (3.65 eV), the RMS system noise, and correction term, respectively. The free parameters are N, $\frac{F}{W}$, and A. Although the physical interpretation of A is not clear, this phenomenological model can fit the XIS data well. We achieve a (pre-flight) energy resolution of $\sim$ 130 eV at 5.9 keV for all the sensors and segments.

4.4. Charge Injection Capability

One of the major advantages of the XIS over ASCA, Chandra and XMM is the provision of a precision charge injection (CI) capability (Bautz et al. 2004). Details of the CI structure and its electrical performance are presented in LaMarr et al. (2004) and Prigozhin et al. (2004). The

CI can mitigate the effects of in-flight radiation damage in two ways (Gendreau 1995). First, a sufficient quantity of charge periodically injected in each column will fill radiation-induced traps (referred as *sacrificial charge*) in the read-out process (Gendreau et al. 1995). Thus following charge packets produced by X-rays will lose fewer electrons to traps. The effectiveness of this process depends on the relation between the re-emission time from the trap and the read-out rate, so its impact will be different in different XIS clocking modes.

Second, the CI can be used to estimate the column-to-column variation in charge transfer inefficiency (CTI) via the accurate measurement of the charge transfer losses as a function of signal packet size (amount of charge). This requires that the amount of injected charge is reasonably precise compared to that of the X-ray induced charge.

We have verified these CI capabilities using a test CCD equivalent to the FI CCDs of the XIS. A portion of the test CCD was irradiated at room temperature by 40 MeV protons, to a total flux density of 2.0×10^9 cm^{-2}, which is the expected dose at the XIS CCDs after roughly 1.5 to 2 years in the Suzaku orbit. The overall energy resolution in the radiation damaged area (roughly 500 rows across) decreases to 210 eV (FWHM) at 5.9 keV from ∼130 eV of the undamaged area. Details of the verification procedure and the results are given in Bautz et al. (2004) and Prigozhin et al. (2004). Brief summaries of these results follow. These results were obtained in normal clocking mode (8-sec exposures) with neither burst nor window option. We have not yet determined the effects of charge injection in other clocking modes. (1) If charge is injected in every 54th row, then the energy resolution is improved to 144 eV (at 5.9 keV), which is within 10% of the initial (undamaged) resolution of ∼130 eV. (2) The CI technique measured column-to-column CTI variations. The column-averaged PHs for 5.9 keV X-rays show a broad (column-to-column) distribution of ∼ 160 eV (FWHM), and exhibit a tail to low energy. That is, the column-to-column CTI variations alone contribute about 160 eV (FWHM) to the spectral resolution of the device. This means that almost all of the radiation-induced increase in FWHM arises from these column-to-column CTI variations. After correction of the column-to-column CTI variations, however, the contribution to the FWHM is reduced to 65 eV (FWHM). This fully accounts for the observed, post-correction resolution at 5.9 keV of ∼140 eV (FWHM). Since the CI requires significant modification of the data analysis software, we have not yet applied it on-orbit. Since the CI is essential to maintain XIS performance after one year operation, we will soon apply the CI technique on-orbit.

5. Flight Data Processing on the Ground

Although some X-ray event selection processes are carried out on-board, final selection and screening are performed on the ground. The X-ray selection method is essentially the same as that used in the ASCA data, and in the pre-flight calibration: the pixel patterns or the ASCA grades are assigned on the ground. If an event belongs to grade 0, 2, 3, 4 or 6, it is regarded as an X-ray. Grade 7 events, in which the pixel pattern contains more than the 2×2 pixels are regarded as background events. Subsequent on-ground processing steps are described in the following subsections.

5.1. Charge Trail and CTI corrections

During the transfer from the IA to the read-out node, a small fraction of the charge in a pixel is left behind (trailed) to the next pixel in the same column (opposite direction of transfer). Thus some charge confined in a 2×2 pixel (X-ray event) may leak to the outer pixels and then be (incorrectly) regarded as a grade 7 event (background event). The amount of trailing charge is proportional to the number of transfers and depends on the X-ray energy. This charge trail is corrected on ground.

The CTI has increased since launch due to the irradiation of charged particles on-orbit. We have continuously measured the center energy and FWHM of the main peak from the two ^{55}Fe calibration sources. These calibration sources illuminate CCD segments A and D at the corners opposite the read-out nodes. Figure 11 shows the on-orbit time history of the center energy of the main peak. The apparent linear trend is due to charge loss caused by gradually increasing CTI.

The CTI depends on the incident PH as PH$^{-\alpha}$. We have measured α using a variety of techniques, using a variety of data obtained on the ground (Prigozhin et al. 2004) and in-orbit from both the onboard ^{55}Fe and celestial sources. At present, all of these technique yield the value of α in the range 0.1 – 0.3. We expect to determine α more precisely as the mission progresses.

Both the charge trail and CTI increase with time on-orbit, so we up-date the relevant correction parameters regularly to keep the absolute energy error within ±0.2 % at the iron Kα energy and within ±5 eV below 1 keV. The long-term monitoring on-orbit shows that the systematic gain error (at 5.9 keV) is better than 0.1%, presumably limited by systematic errors in the dark-level determination (LaMarr et al. 2006).

Figure 12 shows the time history of the energy resolution of the main peak of the calibration line. The degradation of the energy resolution with time is not currently well-enough studied to implement in the response function. Therefore even for intrinsically narrow lines, apparent line broadening may appear as is shown in figure 13. We note, however, that the spectral resolution plotted in figure 13 is measured at the edge of the detector. The resolution is slightly better at the center of the array, where most targets are imaged, because events detected at the center of the array experience fewer charge transfers.

5.2. Contamination correction

The OBF may be gradually contaminated in time by out-gassing from the satellite. The contamination rate after the XIS door-open is unexpectedly high, and the rate is different from sensor to sensor. Moreover, the thickness of the contamination varies with position on the OBF.

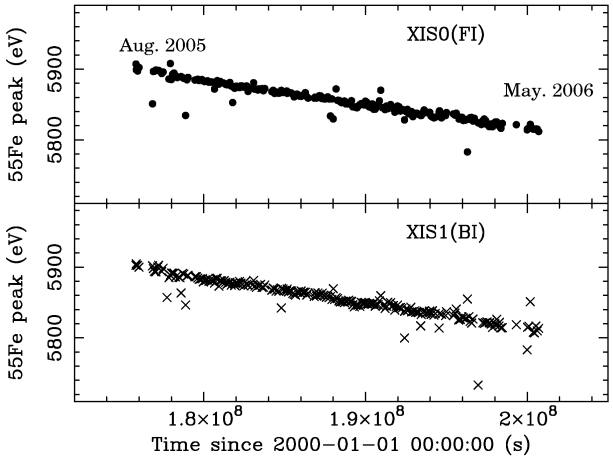

Fig. 11. The time history of the center energy of Mn Kα line from the ^{55}Fe calibration sources for XIS0 (FI: upper) and for XIS1 (BI: lower).

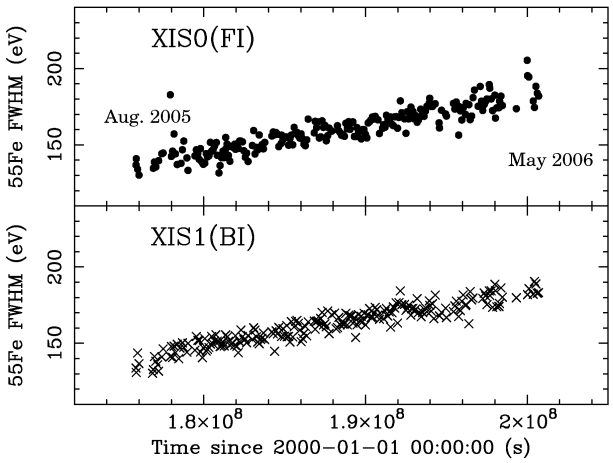

Fig. 12. Same as figure 11, but for the energy resolution (FWHM).

The contamination has caused a significant reduction in low-energy response since launch. We therefore need to include additional, time-varying low energy absorption in the response function. This is given as a function of both the observation date after the XIS door-open, and of detector coordinates (specifying the position on the OBF). For this purpose, we measured the on-axis extra absorption by observing a SNR 1E0102−72 and an isolated neutron star RX J1856.5−3754. At the time of writing, we have not conclusively determined the chemical composition for the contamination material(s). From the overall spectral shape in the low energy absorption for all the available X-ray sources and the best guess for the outgassing source in Suzaku, we assume that the contaminant contains predominantly C and O with the number ratio C/O ~ 6. Figure 14 shows the time histories of the contamination accumulated on the OBF. Empirically, the time dependence of the contamination thickness is assumed to follow the exponential form as;

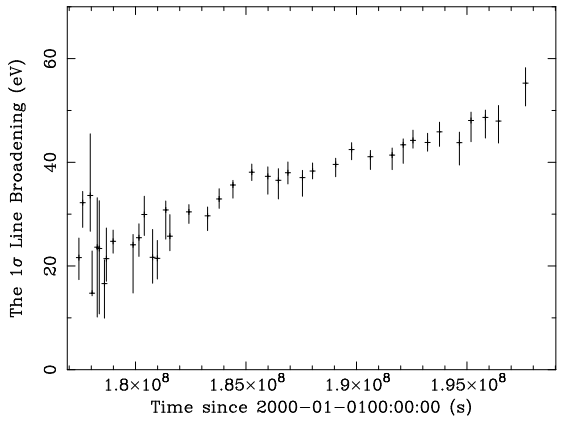

Fig. 13. The line broadening, expressed as the standard deviation of a Gaussian kernel which must be convolved with the current assumed response function to match the observed response, at 5.9 keV (Mn Kα line), of XIS0 after the CTI correction. Note that the line broadening is an artificial effect due to degrading energy resolution in time. At the center of the array, where most targets are imaged, the line broadening is slightly smaller than shown here.

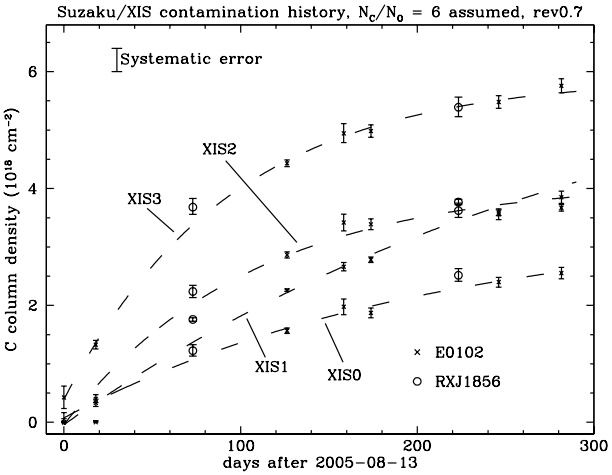

Fig. 14. The time history of the contamination of all four XIS detectors, measured at the center of the OBF.

$$N_{\rm C} = a - b \times \exp(-day/c) \ ,$$

where $N_{\rm C}$ is the carbon column density in units of 10^{18} cm^{-2} (C/O = 6) [3].

To measure the off-axis absorption, we used diffuse X-rays from the bright Earth rim and the Cygnus Loop. The former emits characteristic Kα lines of N I and O I (neutral atoms) and the latter provides Kα lines from C VI, N VII, O VII and O VIII (He-like or H-like atoms). Since the for-

[3] The current response function contains a different functional form with the temporal evolution of the contamination: $N_{\rm C}$ is a piecewise-linear function of time with a change in slope in December 2005

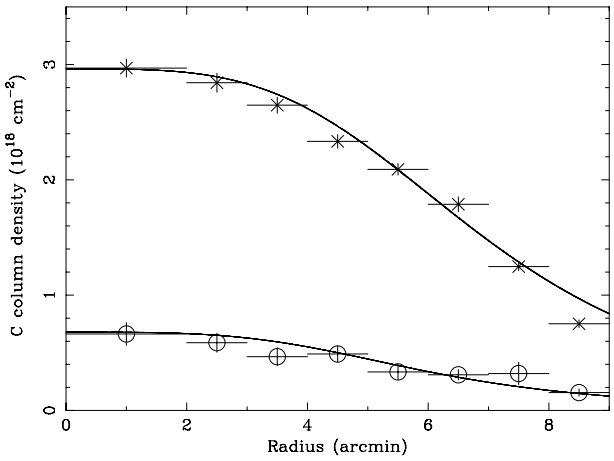

Fig. 15. The radial profile of the contamination of the BI (XIS1). The circles and crosses represent the data for one month and five months after the door-open, respectively.

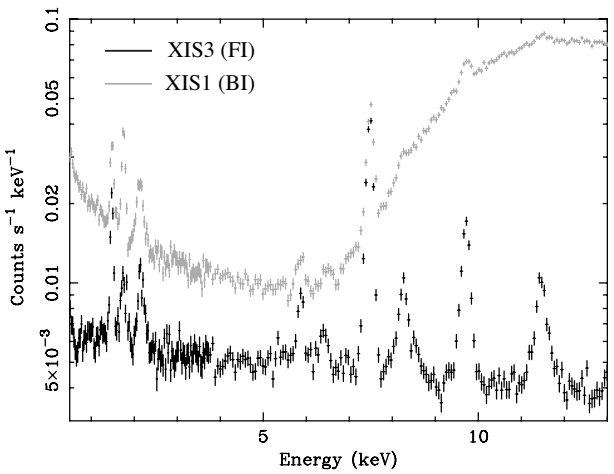

Fig. 16. The night Earth spectra with the BI and FI CCDs.

mer can be observed frequently, we trace the time history of off-axis absorption over successive one-month periods after the XIS door-open (13 August, 2005). With the two reasonable assumptions that (1) the N:O line flux ratio is uniform over the field of view and (2) the contamination is azimuthally constant, we can derive the radial profile of the difference of contamination thickness from the center value. We show the radial profiles of the column density of carbon in figure 15 for one month and five months after the door-open. This radial profile is approximated by a function of $1/[1+\{r/a(t)\}^{b(t)}]$. The time dependent parameters, $a(t)$ and $b(t)$ are determined and up-dated regularly.

6. On Orbit Performance

Since the Suzaku launch on 10 July, 2005, the XIS has been working properly. In this section, we briefly report initial results from the XIS, which demonstrate its low non-X-ray background (NXBG) and good energy resolution over a wide spectral band, in particular from diffuse sources.

Figure 16 shows the NXBG spectra of FI and BI sensors when the XIS observes the dark (night) Earth. The data obtained during the passage thorough the SAA and events in the calibration source area (the 2 corners) have been excluded. The lines at 5.9 keV and 6.5 keV are due to scattered X-rays from the calibration sources. Other than these, many lines, Kα of Al, Si, Ni and Kβ of Ni and Lα, Lβ and Mα lines of Au are detected. Thanks to the low-Earth orbit of Suzaku, the NXBG is fairly low, especially for the FI CCDs.

The NXBG in the 0.5–10 keV band is about 8×10^{-8} counts s^{-1} pix^{-1} (for the FI: XIS0, 2. and 3) and 2×10^{-7} counts s^{-1} pix^{-1} (for the BI: XIS1). The flux of NXBG depends on the cut-off rigidity (COR): the FI fluxes in the 0.4–12 keV band are about 0.2 counts s^{-1} and 0.1 counts s^{-1} for the COR of 4–6 GV and 12–14 GV, respectively, while the BI fluxes in the same COR band are about 0.6 counts s^{-1} and 0.3 counts s^{-1}, respectively. Thus for the most accurate NXBG subtraction, the data should be selected so that the COR distribution of the NXBG observation is the same as that in the source observation. However, given the low NXBG, great concern on the COR is not necessary for most of the XIS observations.

The performance in the low energy band of the BI CCD is demonstrated in figure 17, which shows the spectrum of the young SNR 1E 0102−72. Note that Kα lines of O VII and O VIII at 0.57 and 0.65 keV are clearly resolved. Also note that no low energy tail below the O VII line is found in either BI or FI. In the low energy band (below about 0.4 keV), the BI CCD provides quantum efficiency more than 10 times better than the FI, and with comparable spectral resolution. This spectral resolution performance is the best yet achieved with a BI, photon-counting X-ray CCD in space.

Figure 18 is the hard X-ray spectrum from our Galactic center region, where the NXBG has been subtracted. We see that three Kα lines from Fe I (6.4 keV), Fe XXV (6.7 keV) and Fe XXVI (6.9 keV) are nicely resolved. In addition, Kα lines of Ni I and Ni XXVII, Kβ lines of Fe I, Fe XXV and Fe XXVI, and even Kγ lines of Fe XXV and Fe XXVI are found above ∼7 keV (Koyama et al. 2006). This demonstrates reliable NXBG subtraction and superior energy resolution. These capabilities of the XIS enable us to perform line-resolved imaging studies even of low surface brightness sources.

7. Summary

The XIS design, fabrication, data processing, ground calibration and on-orbit performance for about one year of Suzaku operation may be summarized as follows:
(1) We have prepared four XIS sensor systems; three contain FI CCDs and the other has a BI CCD. The XIS has been working properly on board Suzaku.
(2) The thickness of the depletion layer of the FI CCD is ∼65 μm, while that of the BI is ∼42 μm, hence quantum efficiency of the BI at high energy is lower than that of

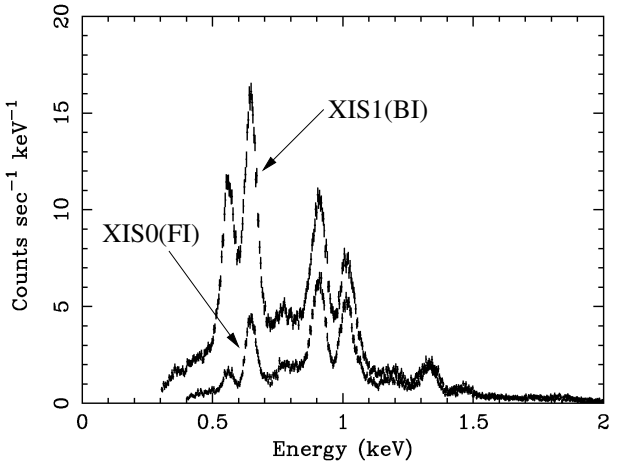

Fig. 17. The X-ray spectra of 1E 0102−72 with the BI and FI CCDs. The BI provides high quantum efficiency at the Kα lines of O VII (0.57 keV) and O VIII (0.65 keV), and also exhibits excellent spectral resolution with small low energy tail, comparable to that of the FI.

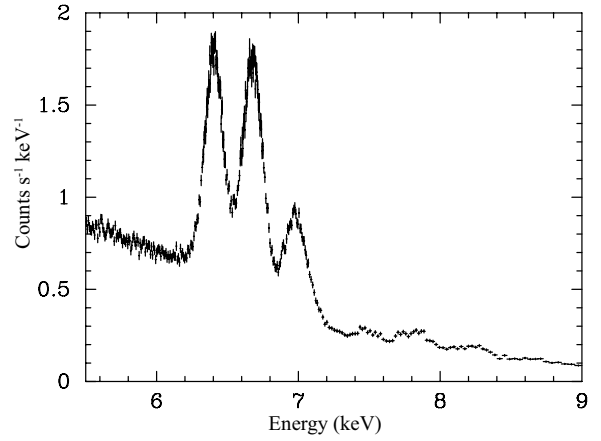

Fig. 18. The X-ray spectrum of the Galactic Center. The four XIS data are added. The night Earth background is subtracted.

the FI.
(3) Each XIS exhibits moderate energy resolution (130 eV, FWHM at 5.9 keV), and low background of charged particles. The BI CCD has nearly the same quality response function as that of the FI CCDs.
(4) We successfully operate the TEC to control the CCD temperature at −90 °C, significantly lower than the ASCA SIS.
(5) The combination of clocking modes and editing modes allow great flexibility in data collection.
(6) A charge injection (CI) mechanism is implemented in the XIS CCD. In the laboratory, we found it to work as a column-to-column CTI monitor as well to compensate for CTI by injecting *sacrificial charge* in radiation-induced traps. The CI technique will be soon applied on-orbit.
(7) The BI CCD (XIS1) is found to exhibit excellent energy response even in the low energy band containing the C, N, and O K-shell transition lines. This is due to a successful application of chemisorption charging back-side treatment process.
(8) We have experienced unexpectedly large contamination on the XIS OBFs, which has caused significant decrease of low energy efficiency. Using low energy sources and day Earth data, we are monitoring the time history of the thickness of the contamination. The thickness is largest at the OBF center and becomes smaller at the periphery. We have made a semi-empirical model to represent the time- and position-dependent contamination.

Suzaku is a re-flight mission of Astro-E, which has started more than 15 years ago. Since then many graduate students have been involved in this long project. The authors sincerely thank the former graduate students, S. Ueno, K. Imanishi, K. Yoshita, K. Hashimotodani, K. Katayama, M. Shouho, K. Mori, T. Shiroshoji, and M. Shoji for their early phase contributions on the ground experiments of the XIS. We also thank all the Suzaku team members and associated graduate students, especially Y. Hyodo, T. Inui , N. Ota, A. Kubota, Y. Takei, K. Sudoh, A. Sekiguchi, D. Takei, and T. Ogita for their support, help and useful information about the on-orbit calibrations.

References

Bautz, M. W., et al. 2000, Proc. SPIE, 4012, 53.
Bautz, M. W., Kissel, S. E., Prigozhin, G. Y., LaMarr, B., Burke, B. E., & Gregory, J. A. 2004, Proc. SPIE, 5501, 111
Born, M, & Wolf, E. 1999, "Principles of optics" seventh edition, Cambridge University Press, Cambridge, UK, p67
Burke, B. E., Mountain, R. W., Harrison, D. C., Bautz, M. W., Doty, J. P., Ricker, G. R., & Daniels, P. J. 1991, IEEE Trans. ED-38, 1069
Dotani, T., et al. 2003, Proc. SPIE, 4851, 1071
Gendreau, K. C., Prigozhin, G. Y., Huang, R. K., & Bautz, M. W. 1995, IEEE, Transactions on Electron Devices, 42, 1912
Gendreau, K. C. 1995, PhD Thesis (Massachusetts Institute of Technology)
Hayashida, K., et al. 2004, Proc. SPIE, 5488, 73
Hamaguchi, K., Maeda, Y., Matsumoto, H., Nishiuchi, M., Tomida, H., Koyama, K., Awaki, H., & Tsuru, T. G. 2000, Nuclear Instruments and Methods in Physics Research A, 450, 360
Hashimotodani, K., et al. 1998, Rev. Sci. Instr., 69, 3746
Kitamoto, S., et al. 2003, Nuclear Instruments and Methods in Physics Research A, 5168, 376
Koyama, K., et al. 2006, PASJ, 58 in press (# 2922)
LaMarr, B., Bautz, M. W., Kissel, S. E., Prigozhin, G. Y., Hayashida, K., Tsuru, T. G., & Matsumoto, H. 2004, Proc. SPIE, 5501, 385
LaMarr, B., et al. 2006, Proc. SPIE, 6270, in press
Lesser, M., & Lyer, V. 1998, SPIE, 3355, 446
Lumb, D. H., et al. 2000, Proc. SPIE, 4140, 22
Matsumoto, H., et al. 2005, Nuclear Instruments and Methods in Physics Research A, 541, 357
Matsumoto, H., et al. 2006, Proc. SPIE, in press
Mitsuda, K., et al. 2006, PASJ, 58 in press (#2954)

Murakami, H., Tsuru, T. G., Awaki, H., Sakano, M., Nishiuchi, M., Hamaguchi, K., Koyama, K., & Tsunemi, H. 1999, Proc. SPIE, 3765, 160

Nakajima, H., Yamaguchi, H., Matsumoto, H., Tsuru, T. G., Koyama, K., Kissel, S., LaMarr, B., & Bautz, M. W. 2005, Nuclear Instruments and Methods in Physics Research A, 541, 365

Prigozhin, G. Y., Burke, B. E., Bautz, M. W., Kissel, S. E., LaMarr, B., & Freytsis, M. 2004, Proc. SPIE, 5501, 357

Serlemitsos, P., et al. 2006, PASJ, 58 in press (#2926)

Tsuru, T. G., Awaki, H., Koyama, K. Hamaguchi, K., Murakami, H., Nishiuchi, M. Sakano, M., & Tsunemi, H. 2001, in X-ray astronomy : stellar endpoints, AGN, and the diffuse X-ray background, ed. N. E. White, G. Malaguti & G. G. C. Palumbo. (AIP conference proceedings, Vol. 599. ISBN 0735400431, 478)

Weisskopf, M. C., Brinkman, B., Canizaress, C., Garmire, G., Murray, S., & Van Speybroeck, L. P. 2002, Publ. Astron. Soc. Pacific, 114, 1

Yamaguchi, H., et al. 2005, Proc. The X-ray Universe, Madrid, Spain